Journal of Radioanalytical and Nuclear Chemistry (2024) 333:1343–1356
https://doi.org/10.1007/s10967-024-09363-3

Comparison of adsorption of U(VI) by magnetic MCM-41, MCM-48 and SBA-15 mesoporous silicas

Dongxu Bi[1,2] · Weiqian Cai[3] · Lingshan Xiong[3] · Qie Luo[3] · Youqun Wang[1,2,3] · Zhibin Zhang[1,2] · Lin Xu[1,2] · Xiaohong Cao[1,2] · Yunhai Liu[1,2,3]

Received: 1 November 2023 / Accepted: 2 January 2024 / Published online: 4 February 2024

Abstract
Three types of magnetic mesoporous silicas (MMSs), namely, MMCM-41, MMCM-48 and MSBA-15 were prepared by a hydrothermal method using CTAB and P123 as templates. The structure and physicochemical properties of MMSs were characterized by small angle XRD, VSM, ζ potential analyzer, contact angle measurer, and XPS, etc. The potential applications of MMSs in U(VI) recovery were thoroughly investigated. The adsorptive kinetics, thermodynamics, and selectivity of MMCM-41, MMCM-48 and MSBA-15 were compared. The results show that MSBA-15 revealed a high capacity for U(VI) (341.94 $mg \cdot g^{-1}$) and a superior selectivity than MMCM-41 and MMCM-48. The adsorption mechanism was explored by using the relevant adsorption models and XPS. The results indicated that MSBA-15 could be considered a strong candidate for the adsorption and recovery of U(VI) from radioactive wastewater.

Keywords Uranium · Adsorption · Magnetic mesoporous silicas

Introduction

Uranium is a primary and valuable constituent of nuclear fuel of pressurized water reactor [1]. Additionally, U(VI) is a highly toxic and radioactive metal ion [2], even in trace amounts, can harm organs such as the kidneys, liver, and bones [3], etc. Uranium-containing wastewater may have generated during nuclear fuel fabrication including mining, hydrometallurgy, and conversion. Therefore, there is an urgent need to efficiently eliminate and reuse uranium from contaminated water [4].

Among numerous techniques for U(VI) capture, adsorption is considered the most favorable owing to its high effectiveness, simple operation, and lack of secondary pollution. Moreover, fostering a high efficient adsorbent is the key for this certain objective. Mesoporous silicas (MSs) has attracted increasing attentions for their excellent properties, such as remarkable stability, controllable pore diameter, high specific area [2], rich in porosity [5]. Many MSs adsorbents have been applied into recovery of U(VI) from wastewater, including MSs functionalized with phosphonate [6], amidoxime [7], and amino groups [8].

As a kind of nano-adsorbent, the MMs are found to be difficult to recovery from aqueous solution [9]. With strong magnetic responsivity [10], magnetic mesoporous silicas (MMSs) have tremendous potential in the fields of U(VI) adsorption [10–12], which can easily separation from water by an external magnetic field. But, the MMSs matrix applied in removal of U(VI) were different, such as magnetic MCM-41 [2], and magnetic SBA-15 [13].

Herein, the adsorptive performances for U(VI) at MMSs were compared. Firstly, magnetic MCM-41, MCM-48 and SBA-15 were synthesized using a hydrothermal method. The structure and physicochemical properties of three kinds of MMSs were characterized by small angle XRD, VSM, ζ potential analyzer, contact angle measurer, and XPS, etc.

✉ Youqun Wang
wangyouqun@ecut.edu.cn

✉ Yunhai Liu
yhliu@ecut.edu.cn

[1] State Key Laboratory of Nuclear Resources and Environment, East China University of Technology, Nanchang 330013, Jiangxi, China

[2] Engineering Research Center of Nuclear Technology Application (East China University of Technology), Ministry of Education, Nanchang 330013, Jiangxi, China

[3] School of Nuclear Science and Engineering, East China University of Technology, Nanchang 330013, Jiangxi, China

The adsorption mechanism was clarified by using the relevant adsorption models, FT-IR and, XPS.

Experimental

Reagents and instruments

Ferric chloride hexahydrate (AR), chloroacetic acid (AR), sodium fluoride (AR), and anhydrous sodium acetate (AR) were obtained from Shanghai Macklin Biochemical Technology Co., Ltd. P123 (MW 5800) was acquired from Sigma Aldrich (Shanghai) Trading Co., Ltd. Cetyltrimethylammonium bromide (CTAB, AR), Arsenazo III (AR), and TEOS (AR) were sourced from Shanghai Aladdin Biochemical Technology Co., Ltd.

The equipment used in the study included centrifuge (TG12-WS, Shanghai Spectral, China), XRD instrument (D8 ADVANCE, Bruke, Germany), FT-IR spectrometer (Nicolet iS5, Thermo Fisher, USA), FEI-TEM (Tecnai F20, FEI, USA), XPS (K-alpha, Thermo Fisher, USA), Vibrating sample magnetometer (VSM) (7404 type, Lakeshore, China), Particle potential titration analyzer (Stabino, PMX, Germany), and an automatic gas adsorption system (ASAP2020, Micromeritics, USA).

Preparation of magnetic mesoporous silica

Preparation of Fe_3O_4@ SiO_2 (MNPS)

The Fe_3O_4@SiO_2 composite was synthesized using a sol–gel method. 0.30 g of Fe_3O_4 was dispersed in a 70.0 mL ethanol–water solution ($V_{ethanol}/V_{water} = 6/1$). After ultrasonic treatment for 10 min, 2.0 mL of TEOS and 1.0 mL of ammonia solution were introduced. The solution was mechanically stirred at 25 °C for 10 h. Then, wash it with water and ethanol for three times, separate the product with external magnetic field, and dry it at 60 °C.

Preparation of MMSs

The preparation route for the MMSs is illustrated in Fig. 1. Initially, a mixture comprising 1.50 g of MNPS, 50.0 mL of H_2O, and 5.0 mL of $NH_3{\cdot}H_2O$ was subjected to oscillation using an ultrasonic cleaner for 30 min. After adding 10 mL of TEOS, 0.90 g of NaOH, and 0.19 g of NaF, the resulting mixture was then mechanically blended at 25 °C for 2 h. Subsequently, 3.00 g of CTAB was introduced, and the stirring process was continued for an additional 2 h. After thorough mixing, the resulting solution was transferred to a reaction kettle and aged at 100 °C for 48 h. The obtained product was subjected to washing and dried at 60 °C for 12 h. Finally, the product underwent calcination at 300 °C for 3 h to yield the ultimate product MMCM-41. The preparation of MMCM-48 followed the same procedure, with the only difference being the use of 7.0 g of CTAB.

In a separate process, 4.00 g of P123 and 0.05 g of NH_4F were dissolved in 138.0 mL H_2O and 1.2 mL concentrated hydrochloric acid within a three-neck flask. The solution underwent ultrasonication for 10 min after the addition of 0.60 g of Fe_3O_4@SiO_2. Afterthat, 9.0 mL of TEOS was introduced into the flask, and the solution was stirred at 40 °C and then at 100 °C for 24 h each. The resulting filter residue was obtained after washing with H_2O and subsequent dehydration at 60 °C for 24 h. The final product, MSBA-15, was achieved through calcination at 550 °C for 6 h.

U(VI) adsorption experiment

The adsorption properties of the MMSs for U(VI) were investigated using a batch experiment. In a conventional adsorption procedure, 50 mL of U(VI) solution was introduced into a 150 mL conical flask and adjusted to a fixed

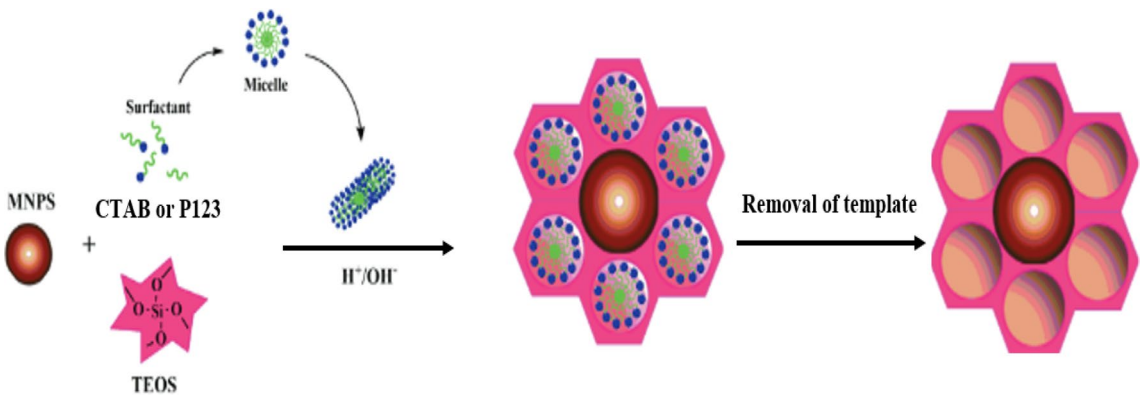

Fig. 1 Schematic synthesis diagram of magnetic mesoporous silicas

pH value with NaOH and HNO_3 solutions. The conical flask with 50 mL solution and 10.0 mg of adsorbent was shaken for a certain time. Then, the U(VI) concentration of supernatant was determined by an Arsenazo III spectrophotometry. Finally, the amount of U(VI) adsorbed [14, 15] (q, $mg \cdot g^{-1}$) and the distribution coefficient [16] (K_d, $mg \cdot mL^{-1}$) were calculated by the Eq. S1 and S2, respectively.

Selective experiment

Weighed amounts of $Zn(NO_3)_2 \cdot 6H_2O$, $Co(NO_3)_2 \cdot 6H_2O$, $Sr(NO_3)_2$, $Pb(NO_3)_2$, $Ni(NO_3)_2 \cdot 6H_2O$, $Ce(NO_3)_3 \cdot 6H_2O$, $Gd(NO_3)_3 \cdot 6H_2O$, and $La(NO_3)_3 \cdot 6H_2O$ were ultrasonically dissolved in a beaker. And, the mixture with 10 mL of 5 $g \cdot L^{-1}$ U(VI) solution was diluted to 1 L volume by deionized water. The concentration of these ions in the prepared solution was 50 $mg \cdot L^{-1}$. After shaking for 240 min, 10 mL of supernatant was taken and added with 2.5 mL of HNO_3 solution (2 $mol \cdot L^{-1}$). Finally, the residual concentrations of the aforementioned ions were measured using an ICP-AES (ICAP-6300, Thermo Fisher, USA).

Results and discussion

Characterization

The micro morphology and ordered structure of the MMSs were examined using TEM and small angle XRD, respectively. The TEM images of MSBA-15 is shown in Fig. 2a and b. Fe_3O_4 is covered with an ordered SiO_2 layer, whose pore wall is approximately 5.13 nm. The small-angle XRD patterns of three types of MMSs are presented in Fig. 2c. Concerning MSBA-15, the peaks at 0.9°, 1.7° and 2.1° correspond to the (100), (110), and (200) crystal planes, revealing that it has hexagonal structure [17]. The peak of MMCM-48 at 2.4° corresponds to the (100) crystal plane, and the characteristic peak of MMCM-41 and MMCM-48 at 2.1° corresponds to the (200) crystal plane, has a good mesoporous structure [18]. The small-angle XRD results indicate that the structure of MMSs is both mesoporous and ordered.

The surface functional groups of MMSs were analyzed using FT-IR, and the findings are illustrated in Fig. 2d. In the infrared spectra of MMSs, there are typical characteristic peaks of mesoporous silica. The bands at 1041 and 804 $cm^{-1}$are Si–O–Si stretching vibration peaks [19, 20]. The stretching and bending vibration of the hydroxyl group connected to the silica atom appears at 1647 and 3750 cm^{-1}

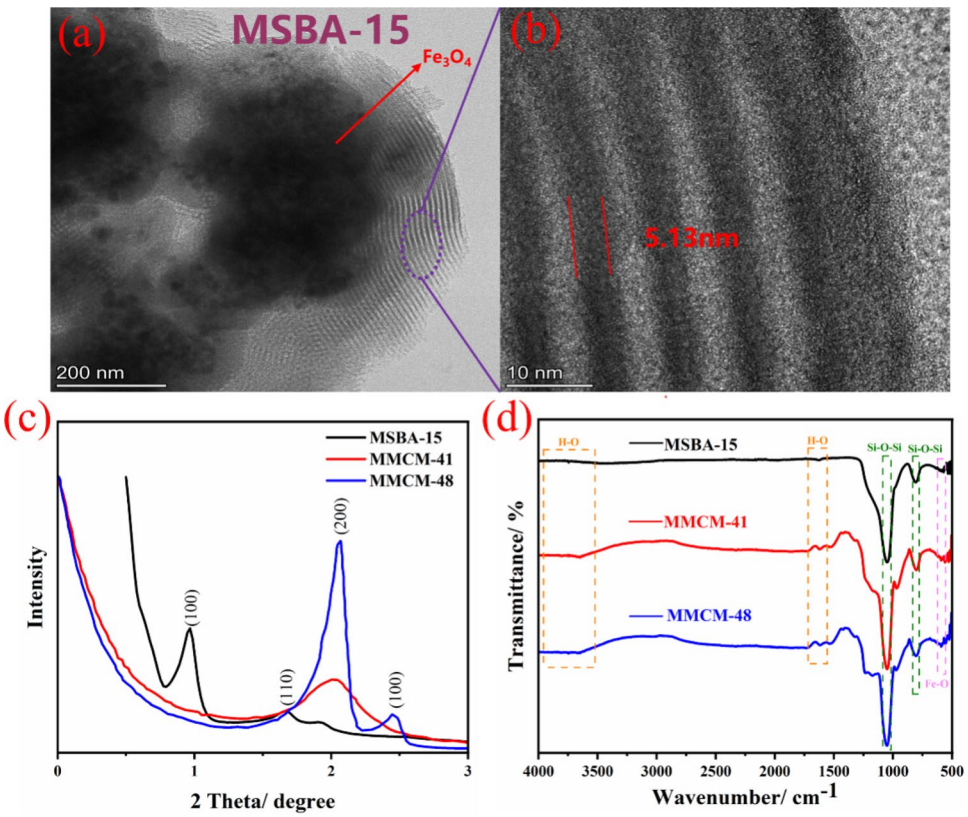

Fig. 2 TEM images of MSBA-15 (**a**)×8×10^5, (**b**)×1.6×10.^{6}, (**c**) small-angle XRD patterns of MSBA-15, MMCM-41 and MMCM-48, (**d**) FT-IR spectra of MSBA-15, MMCM-41 and MMCM-48

[21, 22].The weak absorption peak at about 593 cm^{-1} can be attributed to the vibration of Fe–O bond [23]. The FT-IR results indicate the successful synthesis of three distinct MMSs.

The adsorption–desorption plots were obtained under a N_2 atmosphere. MSBA-15, MMCM-41, and MMCM-48 were degassed at 373.15 K for more than 15 h before the determination. The specific surface of the sample (S_{BET}, $m^2 \cdot g^{-1}$) is calculated from the BET equation [24] at a relative pressure (P/P_0) between 0.05 and 0.25. Pore distribution is calculated by BJH model [25]. In Fig. 3a, the N_2 adsorption–desorption isotherms of MMSs at 77 K. It can be seen from the Fig. that their adsorption isotherms all show the characteristics of type IV curves, indicating that they all conform to the characteristics of mesopores [26]. MSBA-15's type hysteresis ring is a typical H2 type [27], suggesting that it has a narrow mesoporous structure. The N_2 desorption adsorption curves of MMCM-41 and MMCM-48 are H4 type hysteresis loops, showing micro-mesoporous structure. Figure 3b illustrates the BJH pore size distribution of MMSs. The pore size distribution of MMSs is relatively narrow. The most probable pore diameters of MSBA-15, MMCM-41, and MMCM-48 is 8.36, 3.79, and 2.75 nm, respectively. The pore structure data are itemized in Table 1. The S_{BET} and average pore diameter values of MSBA-15, MMCM-41 and MMCM-48 was 675.50, 605.38 and 638.70 $m^2 \cdot g^{-1}$; 6.69 nm, 3.60 nm and 3.56 nm, respectively.

Magnetic properties of MMSs are measured by VSM (Fig. 3c). The magnetic symmetrical hysteresis curves of MSBA-15, MMCM-41 and MMCM-48 all show an S-shape. And, the saturation magnetization is 6.29, 13.66 and 16.17 $emu \cdot g^{-1}$, respectively. Upon the removal of the template from the as-synthesized MSBA-15 at high temperatures, there is a consequential partial oxidation of ferric oxide. It's noteworthy that MSBA-15 can swiftly aggregate using a magnet, as depicted in the inset of Fig. 2c. This property proves beneficial for the recovery of U(VI) through magnetic means.

The ζ potential at different pH values is illustrated in Fig. 3d. The surface potential of the three materials declined with the increasing pH values. Specifically, the surface potential of MSBA-15, MMCM-41, and MMCM-48 decreases from -1.32, 1.53, and 19.83 mV to −48.59, −38.49, and −31.45 mV, respectively, when the pH value is

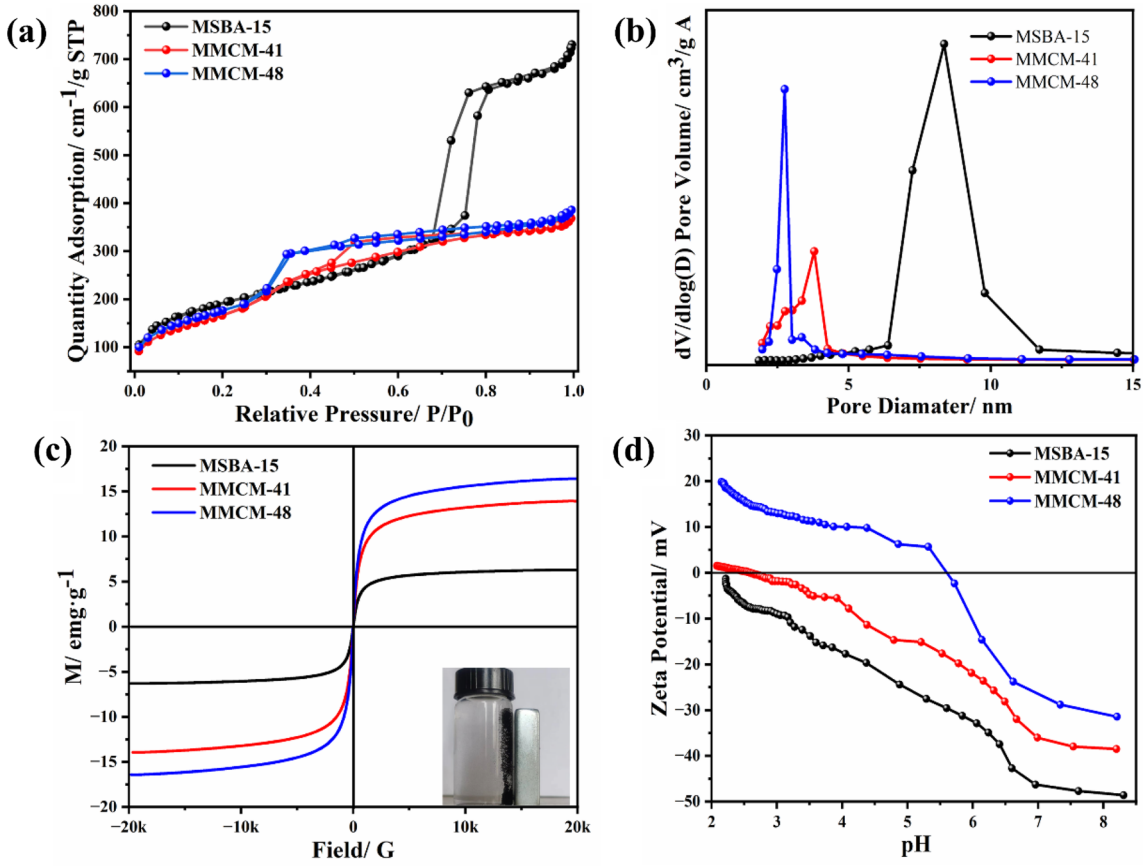

Fig. 3 MSBA-15, MMCM-41 and MMCM-48, (**a**) N_2 adsorption and desorption curves, (**b**) BJH pore size distribution, (**c**) VSM plots, (**d**) ζ potential

Table 1 Pore structure parameters of MSBA-15, MMCM-41 and MMCM-48

Adsorbents	S^{a}_{BET} ($m^2 \cdot g^{-1}$)	V_t^{b} ($cm^3 \cdot g^{-1}$)	V_{meso}^{c} ($cm^3 \cdot g^{-1}$)	D_A^{d} (nm)	D_{BJH}^{e} (nm)	D_m^{f} (nm)
MSBA-15	675.50	1.13	1.13	6.69	8.02	8.36
MMCM-41	605.38	0.54	0.62	3.60	3.27	3.79
MMCM-48	638.70	0.57	0.66	3.56	3.14	2.75

[a]Specific surface area calculated by BET method

[b]Total pore volume

[c]BJH desorption volume

[d]Average aperture, $D_A = 4V_t/S_{BET}$

[e]BJH desorption average pore size

[f]The most probable aperture

within the range of 2.0–8.0. The pH values of the zero potential points (pH_{IZE}) of MMCM-41 and MMCM-48 is 2.6 and 5.6, respectively. When the pH value of the external system exceeds the pH_{IZE} of the material, the surface potential of the material becomes negative. This negative surface potential contribute to the adsorption of U(VI) through electrostatic attraction.

The hydrophilicity of materials was explored through contact angle. Contact angle of MMSs after dropping liquid for 5 s is illustrated in Fig. 4. The contact angles of MSBA-15, MMCM-41, and MMCM-48 was 22.5°, 24.5°, and 31.5°, indicating that MSBA-15 has best hydrophilicity [28]. Excellent hydrophilicity of MSBA-15 facilitates the contact with aqueous solution and improves the separation ability of U(VI) [29].

The XPS was employed to characterize the element composition and chemical form of the prepared MSBA-15 material. The corresponding spectra are shown in Fig. 5. The peaks of Fe, O, C and Si appear in the full spectrum, indicating Fe_3O_4 and mesoporous silica combined together closely. The spectrum peak of Fe 2p shows that Fe $2p_{1/2}$ and $2P_{3/2}$ is located at 708.9 and 714.1 eV, respectively [30]. It signposted that Fe_3O_4 exists in MSBA-15, showing a good match with the results of TEM and FT-IR. The C 1 s peak separation that the synthesized magnetic mesoporous silica material contains two peaks of C–C and C–Si, locating at 284.1 and 282.6 eV, respectively. It noted that the synthesized MSBA-15 also contained a small amount of template that has not been removed completely. Figure 5d is the spectrum of Si 2p, with Si–OH at 102.1 eV and Si–C at 101.4 eV [31]. In the O 1 s spectrum, the peak at 531.3 and 530.5 eV corresponds to Si–OH and O–H. In summary, the XPS analysis corroborates the presence of Fe_3O_4 in MSBA-15. The characterization indicates a substantial presence of silica hydroxide groups on the material's surface.

pH value

The impact of pH value on the adsorption of U(VI) by MSBA-15, MMCM-41 and MMCM-48 was studied in the range of pH 2.0–7.0 ($C_0 = 50$ mg·L^{-1}, $m = 10$ mg, $V = 50$ mL, $T = 298.15$ K, $t = 240$ min). The results are displayed in Fig. 6. Under acidic conditions, U(VI) predominantly exists in the form of UO_2^{2+}. And, the competition of H^+ with U(VI) for the active sites on the MMSs resulted in lower adsorption [32]. With the increasing of pH values, the ζ potential of MMSs decreased according to the Fig. 3d. Consequently, the values of q increased accordingly. At a pH value of 6.0, the adsorption performance of the three types of MMSs for U(VI) reached its peak, with adsorption capacities of 158.18, 126.74, and 125.38 mg·g^{-1}. The best adsorption ability of MSBA-15 may be due to highest pore volume, biggest pore diameter (Table 1) as well as smallest contact angle (Fig. 4). When pH was over 6.0, the anions of $UO_2CO_3(OH)_3^{3-}$ and $UO_2(CO_3)_3^{4-}$ were major components [33]. Thus, the electrostatic repulsion weakened the removal

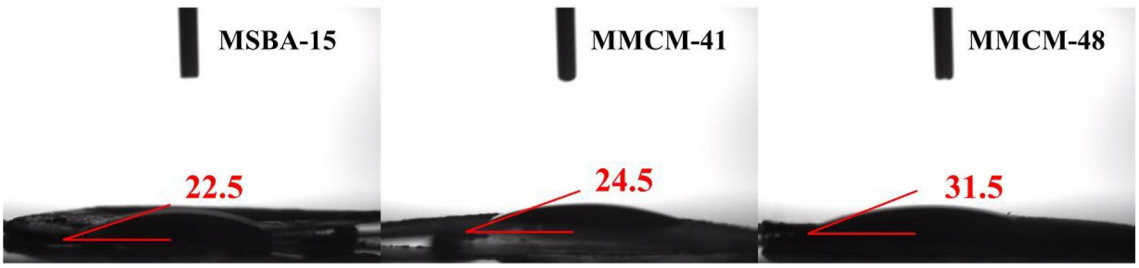

Fig. 4 Contact angle of MSBA-15, MMCM-41 and MMCM-48

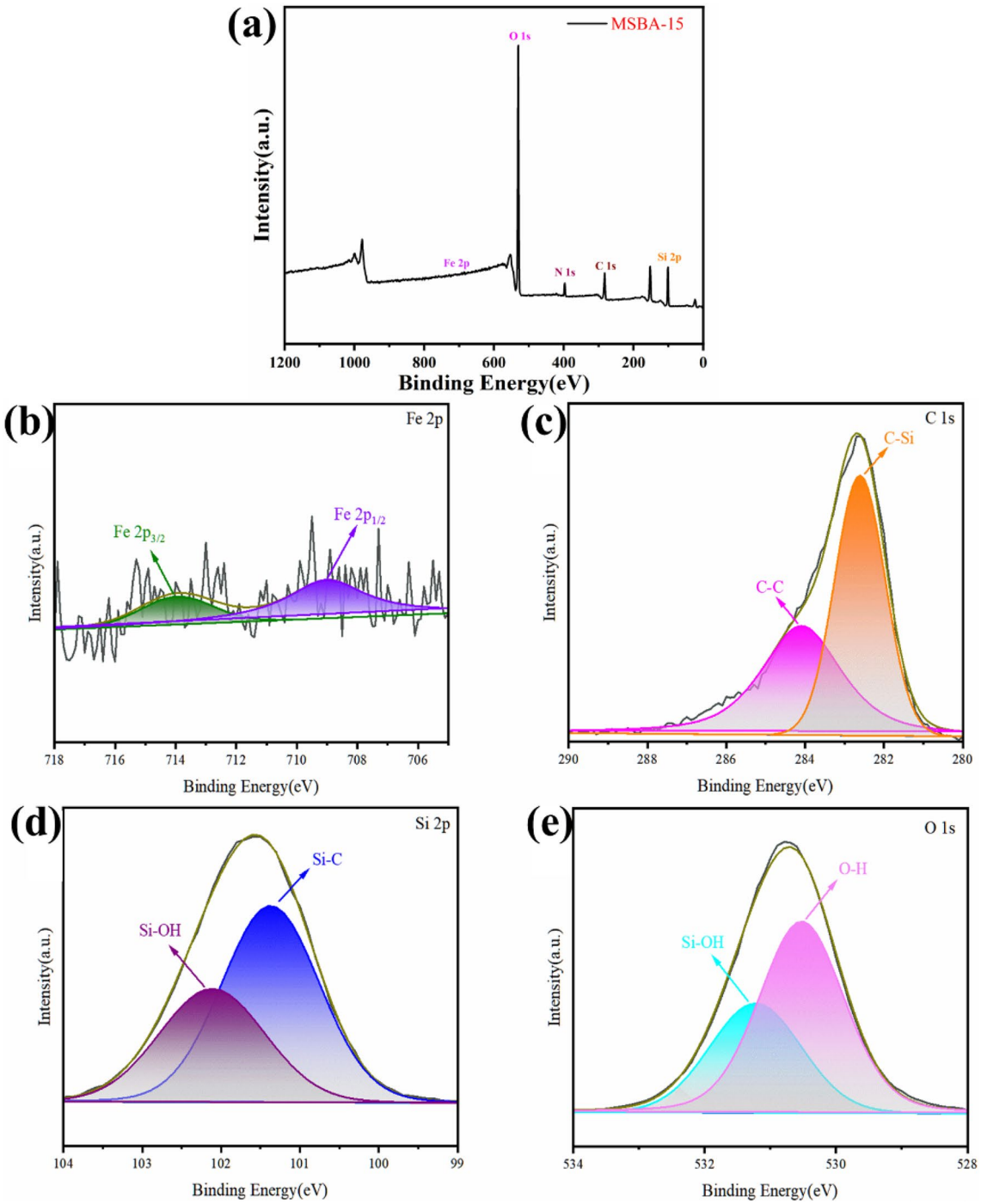

Fig. 5 XPS spectra of MSBA-15: (**a**) survey, (**b**) C 1 s, (**c**) Fe 2p, (**d**) Si 2p, (**e**) O 1 s

capacity for U(VI). As a result, during the subsequent batch experiments, the solution's pH was adjusted to 6.0.

Adsorption kinetics

The effect of contact time on U(VI) adsorption by MMSs ($C_0 = 50$ mg·L^{-1}, $m = 10$ mg, $V = 50$ mL, $T = 298.15$ K, pH = 6.0) was explored. In Fig. 7a, U(VI) rapidly enriched on the surface of MMSs in the initial 90 min. Notably, MSBA-15, MMCM-41, and MMCM-48 achieved adsorption equilibrium at 120, 120, and 240 min, respectively.

Quasi-first order [34, 35], quasi-second order [34] and intra-particle diffusion model [36, 37] were employed to analyze the experimental data and the process of adsorption

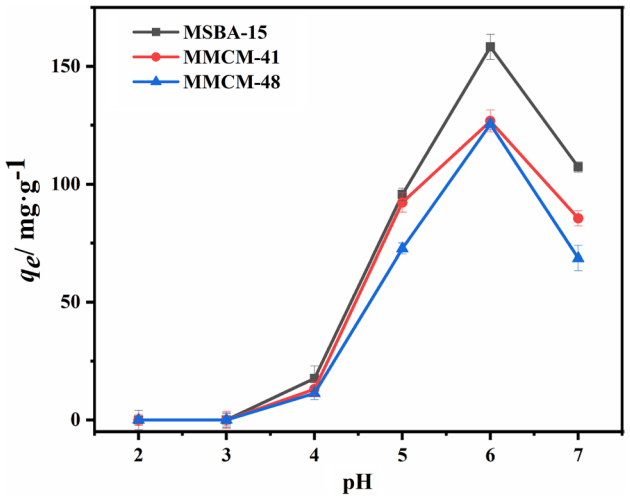

Fig. 6 Effect of pH on the adsorption of U(VI) by MSBA-15, MMCM-41, and MMCM-48 (C_0 = 50 mg·L^{-1}, m = 10 mg, V = 50 mL, T = 298.15 K, t = 240 min)

of U(VI) by MMSs. The formulas of them are shown in form of S3, S4, and S5. The sorption kinetics of U(VI) by MSBA-15, MMCM-41, and MMCM-48 are depicted in Fig. 7a. The fitting parameters are detailed in Table 2. The correlation coefficient (R^2) of the quasi-second order kinetic model for three kinds of MMSs is closer to 1.0. Furthermore, the theoretical adsorption capacity (176.23, 154.86, and 144.33 mg·g^{-1}) is closer to the experimental value (172.40, 152.86, and 140.85 mg·g^{-1}). Consequently, the U(VI) adsorption processes of on MMSs align more closely with the quasi-second-order equation, suggesting that chemical action predominantly governs the adsorption process.

The intra-particle diffusion model [38] of MMSs for U(VI) sorption by MMSs is illustrated in Fig. 7b. The fitting results can be found in Table 3. The internal diffusion rate constants (k_{id}) for the three kinds of MMSs consistently follow the order $k_{id,1} > k_{id,2} > k_{id,3}$, indicating that the adsorption process occurs in three distinct steps.

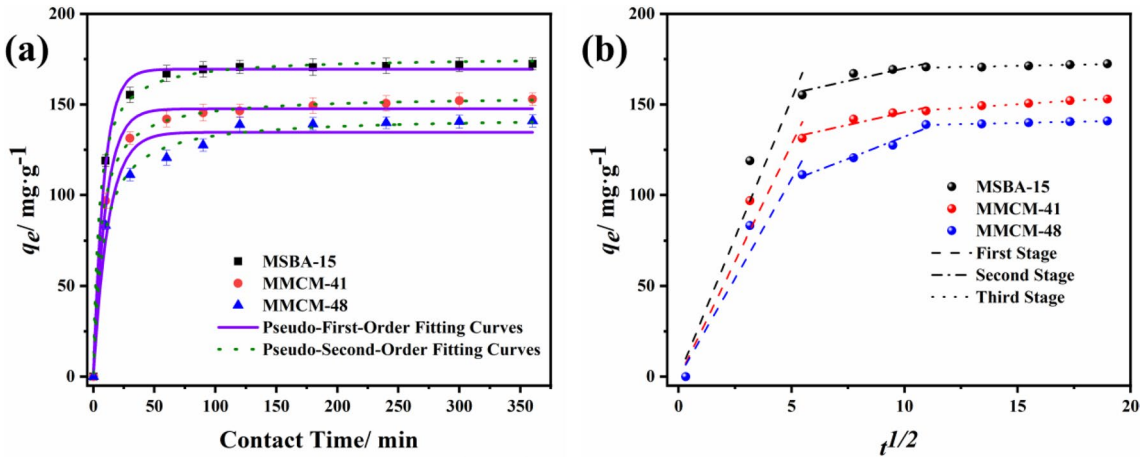

Fig. 7 Fitted curves of (**a**) quasi-primary and quasi-secondary kinetic models for MSBA-15, MMCM-41 and MMCM-48 adsorbed U(VI), (**b**) fitted curves of internal diffusion model (C_0 = 50 mg·L.$^{-1}$, m = 10 mg, V = 50 mL, T = 298.15 K, pH = 6.0)

Table 2 Kinetic parameters of U(VI) adsorption by MSBA-15, MMCM-41 and MMCM-48

Adsorbents	$q_{e,exp}$ (mg·g^{-1})	Quasi-first-order model			Quasi-second-order model		
		$q_{e,cal}$ (mg·g^{-1})	k_1 (min^{-1})	R^2	$q_{e,cal}$ (mg·g^{-1})	k_2 (g·mg^{-1}·min^{-1})	R^2
MSBA-15	172.40	169.49	0.12	0.99	176.23	1.19×10^{-3}	0.99
MMCM-41	152.86	147.59	0.10	0.99	154.86	1.11×10^{-3}	0.99
MMCM-48	140.85	134.67	0.08	0.97	143.33	0.82×10^{-3}	0.99

Table 3 Internal diffusion model parameters for MSBA-15, MMCM-41 and MMCM-48 adsorbed U(VI)

Adsorbents	$K_{id,1}$	C_1	$K_{id,2}$	C_2	$K_{id,2}$	C_2
MSBA-15	30.52	0.28	2.77	142.25	0.24	167.68
MMCM-41	25.77	-0.87	2.77	117.94	0.80	138.08
MMCM-48	21.84	-0.39	4.87	83.49	0.26	135.86

During the initial phase of rapid adsorption, U(VI) in the solution comes into contact with the surface of MMSs and swiftly diffuses towards the material surface. Subsequently, in the slower adsorption process, U(VI) penetrates the inner surface and binds to active sites within. Upon reaching adsorption equilibrium, the diffusion rate approaches 0.

Adsorption isotherm

Figure 8 illustrates the impact of varying equilibrium concentrations of U(VI) (C_e, mg·L^{-1}) on the adsorption efficiency of MMS for U(VI). In the lower concentration range, the adsorption capacity of U(VI) shows a rapid increase. Conversely, at higher concentrations, MSBA-15 demonstrates a gradual attainment of adsorption satiation, reaching a capacity of 319.55 mg·g^{-1}. The saturated adsorption capacities for MMCM-41 and MMCM-48 are 217.88 and 190.54 mg·g^{-1}, respectively.

To further analyze the adsorption processes, Langmuir [39, 40], Freundlich [41], and Sips [42, 43] isotherm models were used. The formula is presented as Eqs. S6, S7, and S8. The fitting results including the values of the R^2 and relevant parameters are revealed in Fig. 8 and Table 4. As shown from Table 7, MSBA-15 exhibit a greater consistency with the Sips adsorption isotherm model with a higher R^2values (0.99) than Freundlich ($R^2 = 0.87$) and Langmuir models ($R^2 = 0.98$). Furthermore, the saturated adsorption capacity (341.94 mg·g^{-1}) obtained by fitting the Sips adsorption isotherm model of MSBA-15 is near to the actual value (319.55 mg·g^{-1}). However, the saturated adsorption capacities of Langmuir adsorption isotherm models for MMCM-41 and MMCM-48

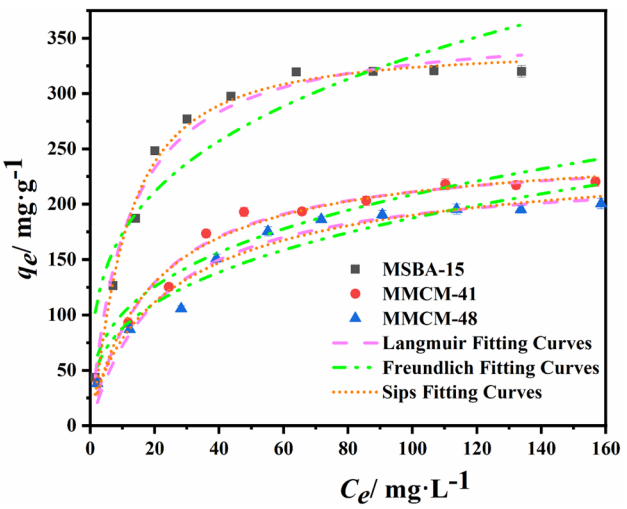

Fig. 8 Langmuir, Freundlich and Sips models for MSBA-15, MMCM-41 and MMCM-48 adsorption U(VI) (m = 10 mg, V = 50 mL, T = 298.15 K, pH = 6.0, t = 240 min)

Table 4 Adsorption isotherm model parameters for U(VI) adsorption by MSBA-15, MMCM-41 and MMCM-48

Model	Parameter	Adsorbents		
		MSBA-15	MMCM-41	MMCM-48
Langmuir	q_e (mg·g^{-1})	362.80	250.60	232.88
	K_L	0.09	0.05	0.05
	R^2	0.99	0.98	0.96
Freundlich	K_F	90.28	49.03	41.31
	1/n	0.28	0.31	0.33
	R^2	0.87	0.92	0.93
Sips	q_s (mg·g^{-1})	341.94	256.72	259.95
	Ks	0.05	0.06	0.07
	c	0.27	0.06	0.20
	R^2	0.99	0.98	0.97
D-R	q_d (mol·g^{-1})	1.49×10^{-3}	1.08×10^{-3}	0.92×10^{-3}
	β	-3.97×10^{-3}	-3.61×10^{-3}	-3.52×10^{-3}
	E (kJ·mol^{-1})	11.18	11.78	11.95
	R^2	0.98	0.97	0.96
Temkin	B (J·mol^{-1})	71.68	46.72	41.86
	K_T	0.70	0.87	0.91
	R^2	0.90	0.96	0.93

(250.60 mg·g^{-1}, 232.88 mg·g^{-1}) are closer to the actual values (217.88 mg·g^{-1}, 190.54 mg·g^{-1}), indicating a single molecular layer adsorption dominated by a chemical process.

To investigate the impact of the initial U(VI) concentration on MSBA-15, MMCM-41, and MMCM-48, the Dubin-Radushkevich (D-R) [44], and the Temkin [45] adsorption isotherm models were employed to compute the binding energy (E, kJ·mol^{-1}) and the constant (B, J·mol^{-1}). The calculation formula for the D-R adsorption isotherm model is represented by Eqs. S9, S10, and S11.

The D-R and Temkin adsorption isotherm models are illustrated in Fig. 9a and b, respectively. The relevant parameters are displayed in Table 4. The values of D-R adsorption isotherm models' R^2 (0.98, 0.97, 0.96) of MSBA-15, MMCM-41, and MMCM-48 are closer to 1. The results are higher than the Temkin adsorption isotherm models (0.90, 0.96, 0.93), presenting that the enrichment of U(VI) by MMSs is more consistent with the D-R adsorption isotherm model. Furthermore, the binding energies of the three kinds of MMSs (11.18, 11.78, 11.95 kJ·mol^{-1}) are all over 8.0 kJ·mol^{-1}. And again, it indicated that adsorption is dominated by chemical reaction [46].

The adsorption capacity of MSBA-15 for U(VI) was compared with that of other adsorbents, and the relevant results are presented in Table 5. Observing the table, it becomes apparent that of MSBA-15 shows a greater saturated adsorption capacity for U(VI) than that of the studied functionalized Fe_3O_4, SBA/SA, MCM-41, and MCM-48, etc.

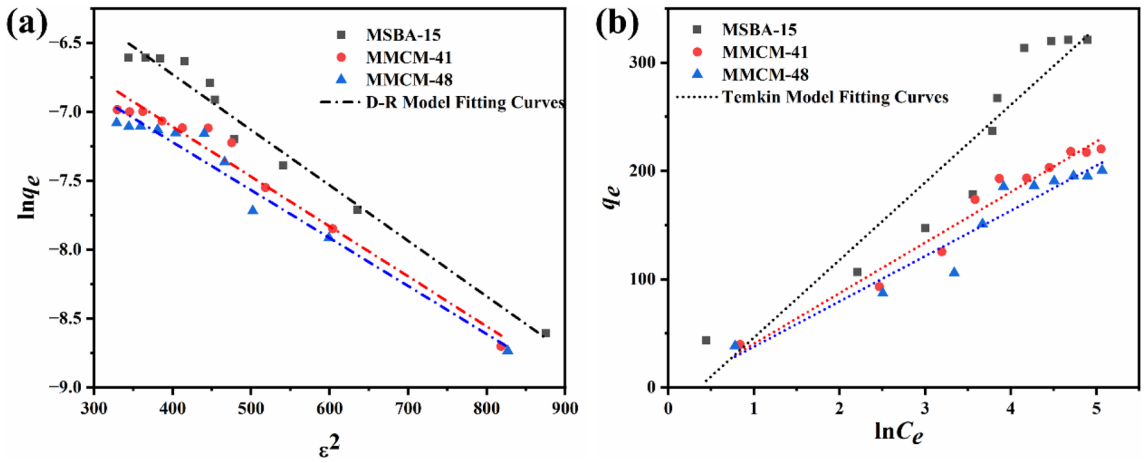

Fig. 9 MSBA-15, MMCM-41 and MMCM-48 adsorption U(VI) isothermal models: (**a**) D-R model; (**b**) Temkin model

Table 5 Comparison of the adsorption performance of different mesoporous material adsorbents on U(VI) at 298.15 K

Adsorbents	Adsorption capacity ($mg.g^{-1}$)	Experimental Conditions	Refs
Phosphoramide functionalized Fe_3O_4	95.2	pH = 6.0	Singhal et al. [47]
Quercetin modified Fe_3O_4@SiO_2	12.3	pH = 3.7	Sadeghi et al. [48]
Functionalized Fe_3O_4@SiO_2	139.1	pH = 5.5	Zheng et al. [9]
Functionalize SBA-15(SBA/SA)	54.1	pH = 4.5	Dolatyari et al. [49]
Functionalize SBA-15 (SBA/EnSA)	105.3	pH = 4.5	
Phnosphonic functional group-based mesoporous silica	207.6	pH = 8.0	Sarafraz et al. [50]
MCM-41	95.0	pH = 6.0	Vidya et al. [51]
MCM-48	125.0	pH = 6.0	
MSBA-15	341.9	pH = 6.0	This work

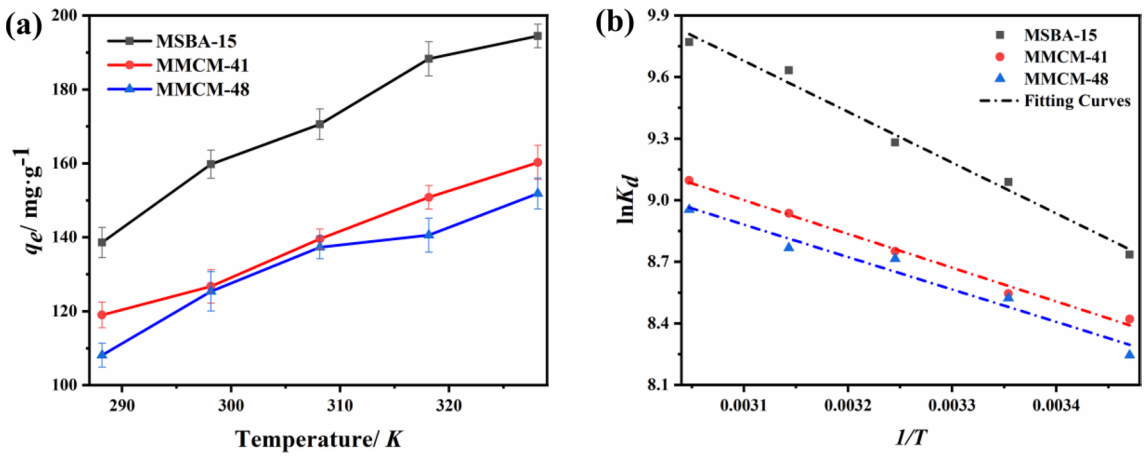

Fig. 10 (**a**) Effect of temperature on the adsorption of U(VI) by MSBA-15, MMCM-41 and MMCM-48, (**b**) thermodynamic curves (C_0 = 50 mg·L.$^{-1}$, m = 10 mg, V = 50 mL, t = 240 min, pH = 6.0)

Table 6 Thermodynamic parameters of adsorbed U(VI) for MSBA-15, MMCM-41 and MMCM-48

Adsorbents	ΔH (kJ·mol^{-1})	ΔS (J·K^{-1}·mol^{-1})	ΔG (kJ·mol^{-1})				
			288.15 K	298.15 K	308.15 K	318.15 K	328.15 K
MSBA-15	20.60	144.33	−20.99	−22.43	−23.87	−25.32	−26.76
MMCM-41	13.67	177.21	−37.39	−39.16	−40.94	−42.71	−44.48
MMCM-48	13.13	114.55	−19.88	−21.02	−22.17	−23.31	−24.46

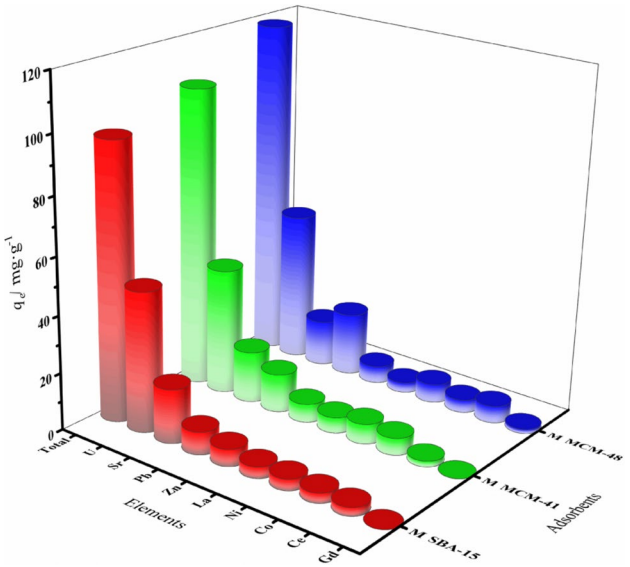

Fig. 11 Selectivity of MSBA-15, MMCM-41 and MMCM-48 for different ions (pH = 6.0, C_0 = 50 mg·L.$^{-1}$, m = 10 mg, V = 50 mL, T = 298.15 K, t = 240 min)

Adsorption thermodynamics

The effect of temperature on the adsorption of U(VI) by MMSs is depicted in Fig. 10a. The equilibrium adsorption capacity of U(VI) increases with rising temperature, suggesting that adsorption of U(VI) is an endothermic process.

To further explore the influence of temperature, the corresponding thermodynamic functions [52] of ΔH, ΔS, and ΔG are calculated by using formulas S13 and S14. Thermodynamic fitting plots are presented in Fig. 10b. According to the results presented in Table 6, $\Delta H > 0$ and $\Delta G < 0$ indicate that the adsorption processes are endothermic and spontaneous.

Adsorption selectivity

The adsorption selectivity of MMSs for U(VI) was studied in the solution with coexisting ions. In Fig. 11, the adsorption capacity of MSBA-15, MMCM-41 and MMCM-48 for U(VI) in the presence of eight ions is 49.03, 44.82 and 52.48 mg·g^{-1}, respectively, accounting for 50.81, 42.89 and 44.47% of the total adsorption capacity. Among them, U(VI) accounts for the largest proportion of MSBA-15 adsorption, thanks to the excellent mesoporous structure and abundant Si–OH of MSBA-15.

To further theoretically evaluate the adsorption selectivity of MMSs for U(VI), the selectivity coefficient (S) [53] is calculated. In Table 7, comparing with the other eight ions, the three MMSs have higher partition coefficients for U(VI), and the selectivity coefficient S is greater than 1, indicating that they can selectively adsorb U(VI) in an aqueous solution.

Table 7 Distribution ratios and selectivity coefficients of MSBA-15、MMCM-41and MMCM-48

Ions	K_d (mL·g^{-1})			$S_{U(VI)/M(x)}$		
	MSBA-15	MMCM-41	MMCM-48	MSBA-15	MMCM-41	MMCM-48
Gd	10.06	10.06	30.30	121.16	106.16	43.33
Ce	60.48	40.16	122.45	20.15	26.59	10.72
Co	71.43	123.71	92.21	17.06	8.63	14.24
Ni	81.14	143.74	133.20	15.02	7.43	9.86
La	81.14	122.25	70.85	15.02	9.51	18.53
Zn	122.95	133.47	122.95	9.91	8.00	10.68
Pb	165.29	285.41	482.46	7.37	3.74	2.72
Sr	411.26	387.93	341.88	2.96	2.75	3.84
U	1218.91	1067.96	1313.13	—	—	—

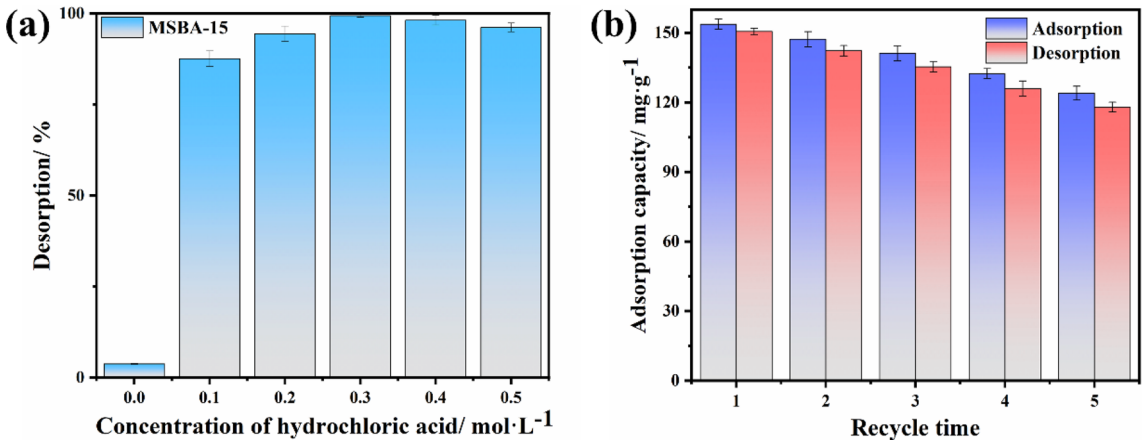

Fig. 12 (**a**) Elution effect of different hydrochloric acid concentrations on MSBA-15, (**b**) reproducibility of MSBA-15

Repetitive experiment

HCl solutions (0–0.50 mol·L^{-1}) are chosen as the desorption solution. Then the reusability experiments of MSBA-15 were carried out (Fig. 12a). The elution rate (D, %) is determined by the formula S16 [54]. The U(VI) adsorbed on MSBA-15 can be eluted with 0.30 mol·L^{-1}HCl with the best elution rate of 99.4%. Thus, 0.30 mol·L^{-1} HCl solution was selected as the eluent for MSBA-15 in subsequent repeated experiments.

Adsorption–desorption-regeneration cycles were repeated for 5 times, as shown in Fig. 12b. After repeating the experiment for 4 times, the adsorption capacity of MSBA-15 for U(VI) decreased to 80.7% of the initial value. It may be related to the destruction of the adsorption active site on MSBA-15. The above results show that MSBA-15 can be reused in recovery of U(VI) from an aqueous solution.

Adsorption mechanism

The potential mechanism of U(VI) adsorption on MSBA-15 was assessed through FT-IR and XPS analyses. In the FT-IR spectrum following the adsorption of U(VI) (Fig. 13a), an asymmetric vibration absorption peak of UO_2^{2+} emerged at 911 cm^{-1}. Furthermore, the stretching and bending vibration peaks (3750 and 1647 cm^{-1}) of the hydroxyl group were intensified.

The XPS spectra of MSBA-15 before and after U(VI) uptake are shown in Fig. 13b. Apart from the Fe 2p, O 1 s, C 1 s and Si 2p peaks, the U 4f peak (Fig. 13c) also manifested in the spectrum after adsorption. It indicated that U(VI) was successfully adsorbed by MSBA-15. Additionally, in the Si 2p spectrum (Fig. 13d), the Si–OH at 102.1 eV shifted to 102.5 eV after adsorption, indicating that there was an interaction between the Si–OH groups and U(VI). In the spectrum of O 1 s (Fig. 13 (e)), the Si–OH peak shifted to 531.3 eV, and the O–H peak at 530.5 eV did not change significantly. In addition, the spectral diagram at C 1 s (Fig. 13f, the C–C peak at 284.1 eV exhibited no change, whereas the C-Si peak at 282.6 eV has shifted. These findings indicate that U(VI) coordinates with the silica hydroxide group on the surface of MSBA-15.

Conclusion

Magnetic mesoporous silicas, MMCM-41, MMCM-48, and MSBA-15, were successfully synthesized. The ordered-mesoporous structure of MSBA-15 was identified by TEM, small angle XRD and N_2 adsorption–desorption curves. The BET specific surface areas of MSBA-15, MMCM-41 and MMCM-48 is 675.50, 605.38 and 638.70 $m^2 \cdot g^{-1}$, respectively. The optimal adsorption pH values of MMSs were all 6.0, and reached adsorption equilibrium within 240 min. MSBA-15 has a higher saturated adsorption capacity (341.94 mg·g^{-1}) and superior selectivity for U(VI) than MMCM-41 and MMCM-48. The adsorption capacity of MSBA-15 for U(VI) decreased to 80.7% of the initial value after 4 recycles. The adsorption of U(VI) on MSBA-15 is mainly the coordination of Si–O–H group with U(VI). In conclusion, MSBA-15 has outstanding performance for U(VI) and is expected to be used in treatment and recovery of U(VI) from radioactive waste water.

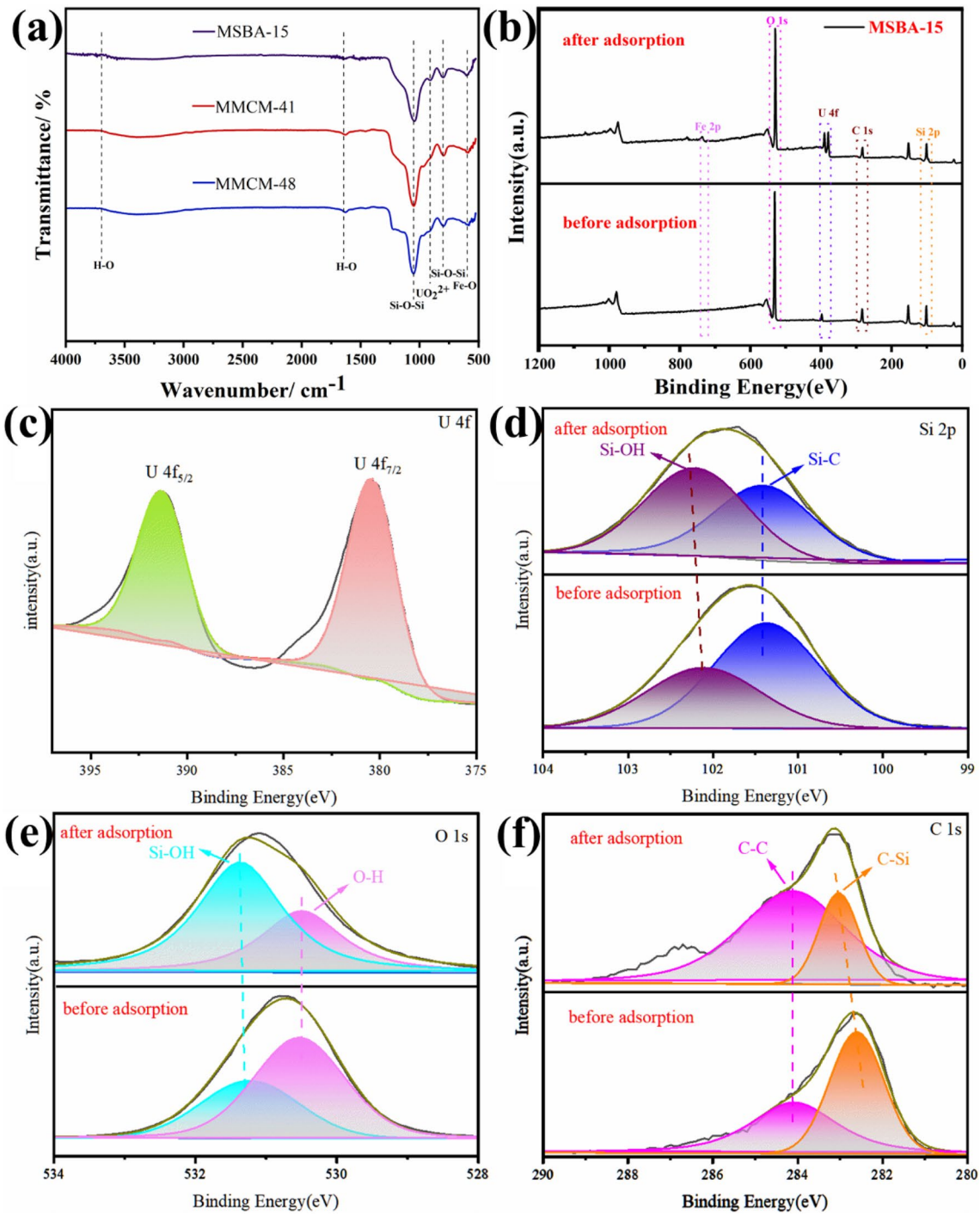

Fig. 13 (a) FT-IR spectrum of MSBA-15 after adsorption, XPS spectra of MSBA-15 before and after adsorption: (**a**) total spectrum, (**b**) U 4f, (**c**) Si 2p, (**d**) O 1 s, (**e**) C 1 s

Supplementary Information The online version contains supplementary material available at https://doi.org/10.1007/s10967-024-09363-3.

Acknowledgements This work was supported by the National Natural Science Foundation of China (22006014, 21906017), Jiangxi Provincial Natural Science Foundation (Grant No. 20202BABL213001).

Authors' contribution DB wrote the entire draft of the manuscript. The core conceptual idea and study design were all provided by YL and YW. The preparation and adsorptive experiments were conducted out with WC and QL. Material preparation and data analysis were completed by XC and LX. The characterization analysis of the adsorbents was worked out through ZZ and LX. WC has revised most of the content of the manuscript according to the comment of reviewers.

Data availability All data generated or analyzed during this study are included in the manuscript.

Declarations

Competing interests The authors declare that they have no competing interests.

Consent to participate Not applicable consent to participate the authors have consent to participate.

Consent to publish Consent to publish the authors have consent to publish.

References

1. Zhu J, Luo Y, Liu J, Liu Q, Yu J, Liu J, Chen R, Li R, Wang J (2023) Effect of fiber surface functionalization on adsorption behavior of uranium from seawater desalination brine. Desalination 564:116774. https://doi.org/10.1016/j.desal.2023.116774
2. Liu F, Huang W, Wang S, Hu B (2022) Investigation of adsorption properties and mechanism of uranium(VI) and europium(III) on magnetic amidoxime-functionalized MCM-41. Appl Surf Sci 594:153376. https://doi.org/10.1016/j.apsusc.2022.153376
3. Amesh P, Venkatesan KA, Suneesh AS, Gupta DK, Ravindran TR (2021) Adsorption of uranium by diethylenetriamine functionalized magnetic mesoporous silica. Environ Nanotechnol Monit Manag 16:100583. https://doi.org/10.1016/j.enmm.2021.100583
4. Xia H, Ren Q, Lv J, Wang Y, Feng Z, Li Y, Wang C, Liu Y, Wang Y (2023) Hydrothermal fabrication of phytic acid decorated chitosan-graphene oxide composites for efficient and selective adsorption of uranium (VI). J Environ Chem Eng 11:110760. https://doi.org/10.1016/j.jece.2023.110760
5. Lewandowski D, Cegłowski M, Smoluch M, Reszke E, Silberring J, Schroeder G (2017) Magnetic mesoporous silica Fe_3O_4@SiO_2@meso-SiO_2 and Fe_3O_4@SiO_2@meso-SiO_2-NH_2 as adsorbents for the determination of trace organic compounds. Microp Mesop Mater 240:80–90. https://doi.org/10.1016/j.micromeso.2016.11.010
6. Giannakoudakis DA, Anastopoulos I, Barczak M, Name D, Terpilowski K, Sigarikar E, Shams M, Coy E, Bakandritsos A, Katsoyiannis I, Colmenares JC, Pashalidis I (2021) Enhanced uranium removal from acidic wastewater by phosphonate-functionalized ordered mesoporous silica: surface chemistry matters the most. J Hazard Mater 413:125279. https://doi.org/10.1016/j.jhazmat.2021.125279
7. Gunathilake CA, Górka J, Dai S, Jaroniec M (2015) Amidoxime-modified mesoporous silica for uranium adsorption under seawater conditions. J Mater Chem 3:11650–11659. https://doi.org/10.1039/C5TA02863A
8. Jiang X, Wang H, Wang Q, Hu E, Duan Y (2020) Immobilizing amino-functionalized mesoporous silica into sodium alginate for efficiently removing low concentrations of uranium. J Clean Prod 247:119162. https://doi.org/10.1016/j.jclepro.2019.119162
9. Zheng H, Zhou L, Liu Z, Le Z, Ouyang J, Huang G, Shehzad H (2019) Functionalization of mesoporous Fe_3O_4@SiO_2 nanospheres for highly efficient U(VI) adsorption. Microp Mesop Mater 279:316–322. https://doi.org/10.1016/j.micromeso.2018.12.038
10. He H, Meng X, Yue Q, Yin W, Gao Y, Fang P, Shen L (2021) Thiol-ene click chemistry synthesis of a novel magnetic mesoporous silica/chitosan composite for selective Hg(II) capture and high catalytic activity of spent Hg(II) adsorbent. J Chem Eng 405:126743. https://doi.org/10.1016/j.cej.2020.126743
11. Li H, Ménard M, Vardanyan A, Charnay C, Durand JO (2021) Synthesis of triethoxysilylated cyclen derivatives, grafting on magnetic mesoporous silica nanoparticles and application to metal ion adsorption. RSC Adv 11:10777–10784. https://doi.org/10.1039/D1RA01581H
12. Li D, Egodawatte S, Kaplan DI, Larsen SC, Serkiz SM, Seaman J (2016) Functionalized magnetic mesoporous silica nanoparticles for U removal from low and high pH groundwater. J Hazard Mater 317:494–502. https://doi.org/10.1016/j.jhazmat.2016.05.093
13. Liu F, Wang A, Xiang M, Hu Q, Hu B (2002) Effective adsorption and immobilization of Cr (VI) and U(VI) from aqueous solution by magnetic amine-functionalized SBA-15. Sep Purif Technol 282:120042. https://doi.org/10.1016/j.seppur.2021.120042
14. Han X, Wang Y, Cao X, Dai Y, Liu Y, Dong Z, Zhang Z, Liu Y (2019) Adsorptive performance of ship-type nano-cage polyoxometalates for U(VI) in aqueous solution. Appl Surf Sci 484:1035–1040. https://doi.org/10.1016/j.apsusc.2019.04.121
15. Chen L, Wang H, Cao X, Feng Y, Zhang Z, Wang Y, Liu Y (2021) Effects of different phosphorus sources on the adsorption of U (VI) by Zr (IV) organophosphate hybrids. J Solid State Chem 302:122434. https://doi.org/10.1016/j.jssc.2021.122434
16. Chen L, Wang Y, Cao X, Zhang Z, Liu Y (2023) Effect of doping cation on the adsorption properties of hydroxyapatite to uranium. J Solid State Chem 317:123687. https://doi.org/10.1016/j.jssc.2022.123687
17. Zholobenko VL, Khodakov AY, Impéror-Clerc M, Durand D, Grillo I (2008) Initial stages of SBA-15 synthesis: an overview. Adv Colloid Interface Sci 142:67–74. https://doi.org/10.1016/j.cis.2008.05.003
18. Lu L, Zhang L, Hu C (2015) Enhanced Fenton-like degradation of pharmaceuticals over framework copper species in copper-doped mesoporous silica microspheres. Chem Eng J 274:298–306. https://doi.org/10.1016/j.cej.2015.03.13
19. Saha B, Singha D, Das T, Nandi M (2023) Tris(4-formyl phenyl)amine functionalized mesoporous silica for selective sensing of Al^{3+} and its separation. Inorganica Chim Acta 550:121455. https://doi.org/10.1016/j.ica.2023.121455
20. Lian J, Liu Y, Chen L, Li L, Ding D, Dai Z (2020) Facile synthesis of calcium peroxide modified mesoporous silica for enhanced uranium extraction from uranium tailings leachate. J Environ Chem Eng 10:108914. https://doi.org/10.1016/j.jece.2022.108914
21. Jia L, Shen J, Li Z, Zhang D, Zhang Q, Duan C, Liu G, Zheng D, Liu Y, Tian X (2012) Successfully tailoring the pore size of mesoporous silica nanoparticles: exploitation of delivery systems for poorly water-soluble drugs. Int J Pharm 439:81–91. https://doi.org/10.1016/j.ijpharm.2012.10.011
22. Zhou C, Yu S, Ma K, Liang B, Tang S, Liu C, Yue H (2021) Amine-functionalized mesoporous monolithic adsorbents for post-combustion carbon dioxide capture. Chem Eng J 413:127675. https://doi.org/10.1016/j.cej.2020.127675
23. Zhang J, Huang L, Ye Z, Zhao Q, Li Y, Wu Y, Zhang W, Zhang H (2020) Removal of arsenite and arsenate from contaminated water using Fe-ZrO-modified biochar. J Environ Chem Eng 10:108765. https://doi.org/10.1016/j.jece.2022.108765
24. López-Pérez L, Zarubina V, Melián-Cabrera I (2021) The Brunauer–Emmett–Teller model on alumino-silicate mesoporous materials. How far is it from the true surface area? Microp Mesop Mater. 319:111065. https://doi.org/10.1016/j.micromeso.2021.111065
25. Wang H, Zhai L, Li Y, Shi T (2008) Preparation of irregular mesoporous hydroxyapatite. Mater Res Bull 43:1607–1614. https://doi.org/10.1016/j.materresbull.2007.06.034
26. Wang GZ, Cao Z, Gu D, Pfänder N, Swertz AC, Spliethoff B, Bongard HJ, Weidenthaler C, Schmidt W, Rinaldi R (2016) Nitrogen-doped ordered mesoporous carbon supported bimetallic PtCo

nanoparticles for upgrading of biophenolics. Angew Chem Int Ed 55:8850–8855. https://doi.org/10.1002/anie.201511558
27. Thommes M, Smarsly B, Groenewolt M, Ravikovitch PI, Neimark AV (2006) Adsorption hysteresis of nitrogen and argon in pore networks and characterization of novel micro-and mesoporous silicas. Langmuir 22:756–764. https://doi.org/10.1021/la051686h
28. Wang Y, Lin Z, Zhu J, Liu J, Yu J, Liu Q, Chen R, Li Y, Wang J (2023) Enhancing adsorption performance and selectivity for uranium by constructing biaxial adsorption sites on eco-friendly bamboo strips. Sep Purif Technol 315:123727. https://doi.org/10.1016/j.seppur.2023.123727
29. Hu H, Gao M, Wang T, Jiang L (2023) Efficient uranium adsorption and mineralization recycle by nano-MgO biochar with superhydrophilic surface. J Environ Chem Eng 11:110542. https://doi.org/10.1016/j.jece.2023.110542
30. Xu J, Liu Z, Li Q, Wang Y, Shah T, Ahmad M, Zhang Q, Zhang B (2021) Wrinkled Fe_3O_4@C magnetic composite microspheres: regulation of magnetic content and their microwave absorbing performance. J Colloid Interface Sci 601:397–410. https://doi.org/10.1016/j.jcis.2021.05.153
31. Acheampong EO, Wang K, Lv R, Lin S, Sun S, Golubev YG, Kotova EL, Kotova OB (2023) Efficient removal of uranium (VI) from aqueous solution by thiol-functionalized montmorillonite/nanoscale zero-valent iron composite. J Radioanal Nucl Ch 332:1989–2002. https://doi.org/10.1007/s10967-023-08847-y
32. Xin Q, Wang Q, Luo K, Lei Z, Hu E, Wang H, Wang H (2024) Mechanism for the seleikctive adsorption of uranium from seawater using carboxymethyl-enhanced polysaccharide-based amidoxime adsorbent. Carbohydr Polym 324:121576. https://doi.org/10.1016/j.carbpol.2023.121576
33. Li Y, Wang Z-Y, Ren Q, Zhang F, Li X-X, Wu Q, Hua R, Yan Z-Y, Wang Y (2023) N, N-bis (2-hydroxyethyl) malonamide based amidoxime functionalized polymer immobilized in biomembranes for highly selective adsorption of uranium(VI). Chemosphere 337:139321. https://doi.org/10.1016/j.chemosphere.2023.139321
34. He Y, Tian H, Xiang A, Wang H, Li J, Luo X, Rajulu AV (2021) Fabrication of PVA nanofibers grafted with octaamino-POSS and their application in heavy metal adsorption. J Polym Environ 29:1566–1575. https://doi.org/10.1007/s10924-020-01865-x
35. Qi L, Teng F, Deng X, Zhang Y, Zhong X (2019) Experimental study on adsorption of Hg(II) with microwave-assisted alkali-modified fly ash. Powder Technol 351:153–158. https://doi.org/10.1016/j.powtec.2019.04.029
36. Fasfous II, Dawoud JN (2012) Uranium (VI) sorption by multiwalled carbon nanotubes from aqueous solution. Appl Surf Sci 259:433–440. https://doi.org/10.1016/j.apsusc.2012.07.062
37. Tao X, Fang Y (2020) Preparation of amidoxime modified calixarene fiber for highly efficient adsorption of uranium (VI). Sep Purif Technol 303:122257. https://doi.org/10.1016/j.seppur.2022.122257
38. Abd El Fatah A, Elashry SM, Hashem M, Kouraim MN (2022) Uranium extraction from nitrate media using amine functionalized poly acrylate hydrogel/nano silica. Sep Sci Technol 57:1187–1197. https://doi.org/10.1080/01496395.2021.1982977
39. Amesh P, Venkatesan K, Suneesh A, Gupta DK, Ravindran T (2021) Diethylenetriamine functionalized silica gel for adsorption of uranium from aqueous solution and seawater. J Radioanal Nucl Ch 329:337–349. https://doi.org/10.1007/s10967-021-07761-5
40. Gado M, Rashad M, Kassab W, Badran M (2021) Highly developed surface area thiosemicarbazide biochar derived from aloe vera for efficient adsorption of uranium. Radiochemistry 63:353–363. https://doi.org/10.1134/S1066362221030139
41. Tian Y, Liu L, Ma F, Zhu X, Dong H, Zhang C, Zhao F (2021) Synthesis of phosphorylated hyper-cross-linked polymers and their efficient uranium adsorption in water. J Hazard Mater 419:126538. https://doi.org/10.1016/j.jhazmat.2021.126538
42. Anirudhan T, Deepa J (2015) Synthesis and characterization of multi-carboxyl-functionalized nanocellulose/nanobentonite composite for the adsorption of uranium (VI) from aqueous solutions: Kinetic and equilibrium profiles. Chem Eng J 273:390–400. https://doi.org/10.1016/j.cej.2015.03.007
43. Lehtonen J, Hassinen J, Kumar AA, Johansson LS, Mäenpää R, Pahimanolis N, Pradeep T, Ikkala O, Rojas OJ (2020) Phosphorylated cellulose nanofibers exhibit exceptional capacity for uranium capture. Cellulose 27:10719–10732. https://doi.org/10.1007/s10570-020-02971-8
44. Gül Üd, Şenol ZM, Gürsoy N, Şimşek S (2019) Effective UO_2^{2+} removal from aqueous solutions using lichen biomass as a natural and low-cost biosorbent. J Environ Radioact 205:93–100. https://doi.org/10.1016/j.jenvrad.2019.05.008
45. Zhou H, Yu J, Liu S, Wang L, Li P (2023) High-efficient uranium-ion adsorption on manganate nanoribbons. Mater Lett 333:133652. https://doi.org/10.1016/j.matlet.2022.133652
46. Smječanin N, Bužo D, Mašić E, Nuhanović M, Sulejmanović J, Azhar O, Sher F (2002) Algae based green biocomposites for uranium removal from wastewater: kinetic, equilibrium and thermodynamic studie. Mater Chem Phys 283:125998. https://doi.org/10.1016/j.matchemphys.2022.125998
47. Singhal P, Vats BG, Yadav AK, Pulhani V (2020) Efficient extraction of uranium from environmental samples using phosphoramide functionalized magnetic nanoparticles: understanding adsorption and binding mechanisms. J Hazard Mater 384:121353
48. Sadeghi S, Azhdari H, Arabi H, Moghaddam AZ (2012) Surface modified magnetic Fe_3O_4 nanoparticles as a selective sorbent for solid phase extraction of uranyl ions from water samples. J Hazard Mater 215–216:208–216. https://doi.org/10.1016/j.jhazmat.2012.02.054
49. Dolatyari L, Yaftian MR, Rostamnia S (2016) Removal of uranium(VI) ions from aqueous solutions using Schiff base functionalized SBA-15 mesoporous silica materials. J Environ Manag 169:8–17. https://doi.org/10.1016/j.jenvman.2015.12.005
50. Sarafraz H, Minuchehr A, Alahyarizadeh G (2017) Synthesis of enhanced phosphonic functional groups mesoporous silica for uranium selective adsorption from aqueous solutions. Sci Rep 7:11675. https://doi.org/10.1038/s41598-017-11993-5
51. Vidya K, Gupta NM, Selvam P (2004) Influence of pH on the sorption behaviour of uranyl ions in mesoporous MCM-41 and MCM-48 molecular sieves. Mater Res Bull 39:2035–2048. https://doi.org/10.1016/j.materresbull.2004.07.013
52. Aslani CK, Amik O (2021) Active Carbon/PAN composite adsorbent for uranium removal: modeling adsorption isotherm data, thermodynamic and kinetic studies. Appl Radiat Isot 168:109474. https://doi.org/10.1016/j.apradiso.2020.109474
53. Zhou L, Shang C, Liu Z, Huang G, Adesina AA (2012) Selective adsorption of uranium (VI) from aqueous solutions using the ion-imprinted magnetic chitosan resins. J Colloid Interface Sci 366:165–172. https://doi.org/10.1016/j.jcis.2011.09.069
54. Zeng J, Zhang H, Sui Y, Hu N, Ding D, Wang F, Xue J, Wang Y (2017) New amidoxime-based material TMP-g-AO for uranium adsorption under seawater conditions. Ind Eng Chem Res 56:5021–5032. https://doi.org/10.1021/acs.iecr.6b05006